2010

High-surface-area -Fe2O3/carbon nanocomposite: one-step synthesis and its highly reversible and enhanced high-rate lithium storage properties

S X. Dou
University of Wollongong, shi@uow.edu.au

David Wexler
University of Wollongong, david_wexler@uow.edu.au

Jiazhao Wang
University of Wollongong, jiazhao@uow.edu.au

Hua-Kun Liu
University of Wollongong, hua@uow.edu.au

Konstantin K. Konstantinov
University of Wollongong, konstan@uow.edu.au

See next page for additional authors

Journal of Materials Chemistry

www.rsc.org/materials

Volume 20 | Number 11 | 21 March 2010 | Pages 2041–2252

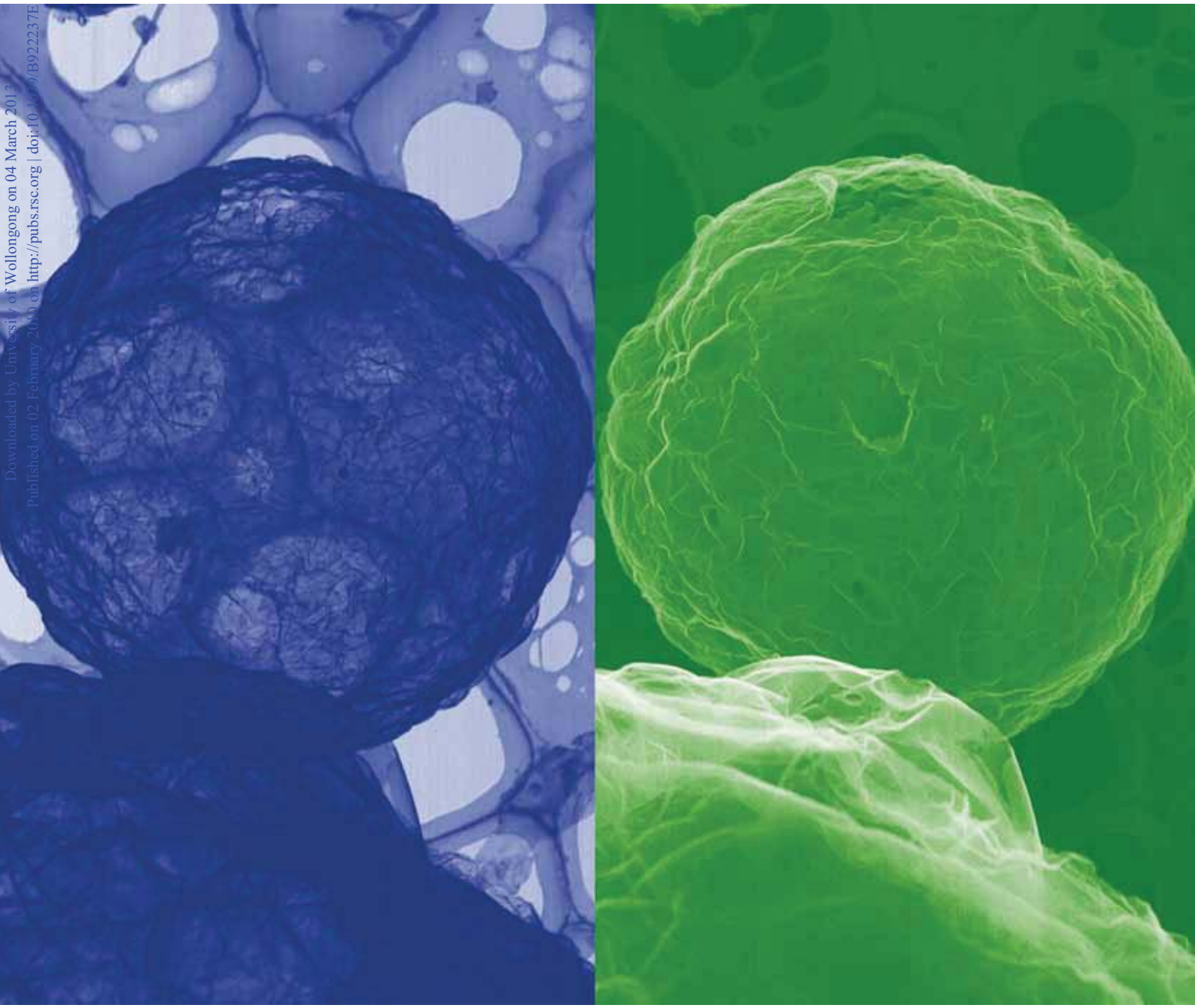

ISSN 0959-9428

RSC Publishing

High-surface-area α-Fe_2O_3/carbon nanocomposite: one-step synthesis and its highly reversible and enhanced high-rate lithium storage properties†

Shu-Lei Chou,*[ab] Jia-Zhao Wang,*[ab] David Wexler,[c] Konstantin Konstantinov,[ab] Chao Zhong,[ab] Hua-Kun Liu[ab] and Shi-Xue Dou[a]

Received 3rd November 2009, Accepted 4th December 2009
First published as an Advance Article on the web 2nd February 2010
DOI: 10.1039/b922237e

Hollow-structured α-Fe_2O_3/carbon (HIOC) nanocomposite with a high surface area of around 260 m^2 g^{-1} was synthesized by a one-step, *in situ*, and industrially-oriented spray pyrolysis method using iron lactate and sucrose solution as the precursors. The small α-Fe_2O_3 nanocrystals were highly dispersed inside amorphous carbon to form a carbon nanocomposite. Electrochemical measurements showed that the carbon played an important role in affecting both the cycle life and the rate capability of the electrode. The HIOC composites showed the best electrochemical performance in terms of high capacity (1210 mAh g^{-1} at a current density of 0.1 C), enhanced rate capability and excellent cycle stability (720 mAh g^{-1} at a current density of 2 C up to 220 cycles). HIOC nanocomposite can also be used in other potential applications, such as in gas sensors, catalysts, and biomedical applications because it is easily dispersed in water and has a high surface area.

Introduction

Lithium-ion batteries are currently the dominant power sources for portable electronic devices and are also considered as promising power sources in electric vehicles (EV) and hybrid electric vehicles (HEV).[1–3] However, the current lithium-ion batteries are approaching limits set by the electrode materials. To improve their energy density, cycling life, and especially, their high-rate capability is the major challenge in next-generation lithium-ion batteries.[2] Due to the low theoretical capacity (372 mAh g^{-1}) of graphitic carbon, which is the most commonly used anode material, intensive research has been conducted to search for alternative anode materials with higher capacities and rate capabilities.[4–6] As one of the promising anode materials, hematite (α-Fe_2O_3) has been investigated intensively due to its great advantages such as high theoretical capacity (1007 mAh g^{-1}), low cost, good stability, environmental friendliness, and high resistance to corrosion.[7–15] Recently, the capacity retention of iron oxide can be improved *via* fabricating active materials into hollow/nano-structures which could accommodate volume changes and shorten the lithium diffusion length.[9,11–14] Furthermore, a selected binder, sodium carboxymethyl cellulose (CMC), can also improve cycling performance of α-Fe_2O_3 at a low current density of 100 mA g^{-1}.[10] It is noticed that almost all the previous reports focused on very low rate charge/discharge current densities (about 0.1 C = 100 mA g^{-1}). It is still a great challenge to improve the high rate capability of iron oxide-base materials.

Generally, the rate capability in a lithium-ion battery system is limited by the transportation of both lithium ions and electrons.[4,16,17] By producing nanostructured materials into/onto a conducting matrix (metal or carbon),[16,18] the high rate capability was significantly improved. However, the available methods involved the usage of templates or a series of procedures which make them unsuitable for industrial applications. Here, we use spray pyrolysis to prepare hollow structured α-Fe_2O_3/carbon nanocomposite in one step. Furthermore, the electrochemical measurements demonstrate that the HIOC composite can be used as a novel anode material in lithium-ion batteries with high capacity, good cycle stability, and high-rate capability.

Experimental

Synthesis

High surface area, hollow-structured, α-Fe_2O_3/carbon (HIOC) nanocomposite with different carbon contents were synthesized by an *in situ* spray pyrolysis method. The detailed parameters are listed in Table 1. The chemicals, including iron(II) lactate hydrate ($C_6H_{10}FeO_6 \cdot xH_2O$, 98%), sucrose ($C_{12}H_{22}O_{11}$, 98%), and HNO_3 (69%), were purchased from Sigma-Aldrich. The precursor solution was peristaltically pumped into a spray pyrolysis furnace with an operating temperature from 600 to 1000 °C using compressed air as the carrier gas. The resultant powder was separated from the hot gas stream *via* a collecting jar, and collected into air-tight sample bottles. The reaction can be simply expressed in the following equation.

$$2C_6H_{10}FeO_6 + C_{12}H_{22}O_{11} + (24.5 - x)O_2 + \text{Heat} \rightarrow Fe_2O_3 + xC\ (\text{amorphous}) + 21H_2O\uparrow + (24 - x)CO_2\uparrow$$

[a]*Institute for Superconducting and Electronic Materials, University of Wollongong, Wollongong, NSW, 2522, Australia. E-mail: sc478@uow.edu.au; jiazhao@uow.edu.au; Fax: +61 2 4221 5730*
[b]*ARC Centre of Excellence for Electromaterials Science, University of Wollongong, Wollongong, NSW, 2522, Australia*
[c]*Faculty of Engineering, University of Wollongong, Wollongong, NSW, 2522, Australia*
† Electronic supplementary information (ESI) available: EDS, FT-IR, TGA, XRD and SEM results. See DOI: 10.1039/b922237e

Table 1 Different HIOC samples prepared under different experimental parameters

	Composition of the precursor solution			
Sample name	Iron(II) lactate/ mol L^{-1}	HNO_3/mol L^{-1}	Sucrose/mol L^{-1}	Pyrolysis T/°C
Sample A	0.25	0.30	0	600
Sample B	0.25	0.30	0	700
Sample C	0.10	0.12	0	700
Sample D	0.50	0.60	0	700
Sample E	0.25	0.30	0.06	700
Sample F	0.25	0.30	0.14	700
Sample G	0.25	0.30	0	800
Sample H	0.25	0.30	0	900
Sample I	0.25	0.30	0	1000

Instrument analysis

The morphology and microstructure of as-prepared samples were characterized by X-ray diffraction (XRD; Philips PW1730), scanning electron microscopy (SEM; JEOL JSM-6460A, 30 kV, equipped with energy dispersive X-ray (EDX) spectroscopy using an indium sample holder), transmission electron microscopy (TEM; JEOL 2011, 200 kV), and Brunauer-Emmett-Teller (BET) equipment (Quanta Chrome Nova 1000). To test the electrodes after cycling, the cells were opened, and the electrodes were taken out, and washed with diethyl carbonate (DEC) 3 times. The thermal properties of the as-prepared hollow α-Fe_2O_3/carbon nanocomposites were characterized by thermogravimetric analysis (TGA; TA Instruments 2000) under air at a flow rate of 40 mL min^{-1} over a temperature range of 80–650 °C with a ramp rate of 5 °C min^{-1}. Raman spectra were recorded using a JOBIN Yvon Horiba Raman Spectrometer model HR800 employing a 10 mW helium/neon laser at 632.8 nm, which was filtered by a neutral density filter to reduce the laser intensity, and a charge-coupled detector (CCD).

Electrochemical characterizations

To test the electrochemical performance, HIOC nanocomposites were mixed with acetylene black (AB) and a binder (sodium carboxymethyl cellulose (CMC, average Mw: ~250 000, Aldrich)) in a weight ratio of 75 : 15 : 10 in de-ionized water. The slurry was uniformly pasted onto pieces of Cu foil with an area of 1 cm^2. Such prepared electrode sheets were dried at 90 °C in a vacuum oven for 12 h. The electrodes were not pressed for electrochemical testing. The electrochemical cells (CR 2032 coin-type cell) contained HIOC nanocomposite on Cu foil as the working electrode, Li foil as the counter electrode and reference electrode, a porous polypropylene film as separator, and 1 M $LiPF_6$ (battery grade 99.99%, Aldrich) in a 1 : 2 (v/v) mixture of ethylene carbonate (EC, anhydrous 99%, Sigma-Aldrich) and diethyl carbonate (DEC, anhydrous 99+%, Sigma-Aldrich) as the electrolyte. The cells were assembled in an Ar-filled glove box. The cells were cycled at a current density of 50 mA g^{-1} (0.05 C) for the first 5 cycles and then cycled at different current densities for the following cycles between 0.01 and 3.0 V using a computer-controlled charger system manufactured by Neware battery testers. The specific capacity is based on the weight of HIOC nanocomposite or HIO sample. The typical loading mass of the electrode material in the electrode is in the range of 4–6 mg cm^{-2}. Cyclic voltammetry (CV) measurements were performed using an Ametek PARSTAT® 2273 electrochemistry workstation.

Results and discussion

Structure and morphologies

Although iron oxide particles have been produced by spray pyrolysis previously using different iron compound precursors, including nitrates,[19] chlorides,[20] and iron pentacarbonyl,[21] the problem is that the materials produced from these precursors show low surface area (less than 50 m^2 g^{-1}). Here, an organic iron salt, iron lactate, was selected as the precursor. Due to the high weight loss from the decomposition of iron lactate (ESI, Fig. S1†), the as-prepared α-Fe_2O_3 or α-Fe_2O_3/carbon composite made from iron lactate is much more porous than that produced from other iron salts.[19–21] Typically, hollow-structured α-Fe_2O_3/carbon (HIOC) nanocomposite was synthesized by the spray pyrolysis method at 700 °C using a precursor solution containing 0.25 M iron(II) lactate, 0.06 M sucrose, and 0.3 M HNO_3. The carbon contents can be easily controlled by adding sucrose into the precursor solution or increasing the reaction temperature. Moreover, the partially oxidized sucrose can lead to the formation of carbon-based materials. For comparison, hollow-structured α-Fe_2O_3 (HIO) with 0% carbon was also synthesized by spray pyrolysis at 1000 °C using 0.25 M iron(II) lactate and 0.3 M HNO_3 as precursors.

The diffraction peaks in the X-ray diffraction (XRD) patterns of HIOC and HIO (Fig. 1a) can be indexed to a rhombohedral α-Fe_2O_3 phase with space group $R\bar{3}c$ (JCPDS no. 79-0007). No peaks of any other phases were detected, indicating the high purity of the α-Fe_2O_3 structures. The crystal size of the HIOC and HIO calculated by the Debye–Scherrer equation applied to the (104) peak is 28.8 and 149.2 nm, respectively. The higher background of the HIOC sample from 20° to 40° is due to the presence of amorphous carbon. The energy dispersive X-ray (EDX) spectrum (ESI, Fig. S2†) confirms that the HIOC composite contains the elements Fe, O, and C, indicating the presence of carbon. Raman spectroscopy (Fig. 1b) confirmed the presence of amorphous carbon with a "G" band around 1600 cm^{-1}, which was not observed in the HIO sample. The peaks below 1400 cm^{-1} are matched very well with the Raman spectrum of α-Fe_2O_3 in the literature.[22] The Fourier transform infrared (FT-IR) spectrum of HIOC composite (ESI, Fig. S3†) shows that the amorphous carbon contains $-COO^-$ functional groups. Thermogravimetric analysis (TGA; Fig. 1c) was used to evaluate the weight percentage of carbon-based materials in the composite. Owing to the good thermal stability of α-Fe_2O_3, the weight loss can be considered as the weight of carbon-based materials in the sample. The carbon-based material in HIO and HIOC composite is calculated from the TGA curves to be 0% and 14.7%, respectively. The specific surface areas of as-prepared products were measured by the 15-point Brunauer-Emmett-Teller (BET) N_2 adsorption method. The specific surface area of HIO and HIOC is 183 and 260 m^2 g^{-1}, respectively, which is

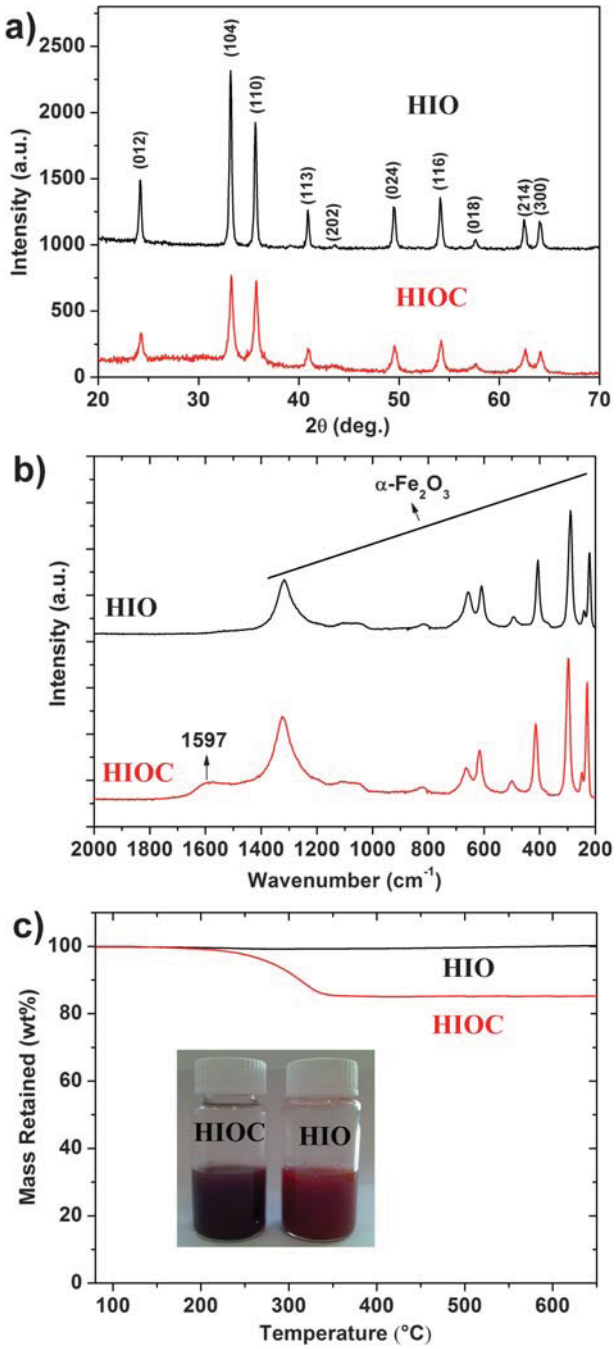

Fig. 1 (a) XRD patterns, (b) Raman spectra and (c) TGA results on as-prepared HIO and HIOC composite *via* spray pyrolysis. The inset of (c) is a photograph of HIOC and HIO samples that were dispersed in water by hand-shaking alone.

much higher than those previously reported for other kinds of α-Fe_2O_3 materials, such as nanotubes (50 $m^2 g^{-1}$),[9] hollow spheres (41.1 $m^2 g^{-1}$),[12] and even mesoporous structures (139 $m^2 g^{-1}$).[23] In addition, the as-prepared HIO and HIOC can be dispersed in water or other solvents by simply shaking. The dispersion of the HIO and HIOC in water can last for more than 1 h without precipitation, as shown in the inset of Fig. 1c. The easy dispersion of HIO and HIOC makes these materials even more promising for potential applications such as in catalysts, water purification, and biomedical applications.

Typical scanning electron microscope (SEM) and transmission electron microscope (TEM) observations of HIOC and HIO samples are shown in Fig. 2. A low magnification SEM image of HIOC (Fig. 2a) shows a large area of hollow sphere-like structures about 1–10 μm in diameter. A higher magnification SEM image of the HIOC composite (inset of Fig. 2a) displays a broken hollow sphere with hierarchical hollow structures. The walls of the hollow structures are composed of very thin nanosheets around 10–20 nm in thickness, which can account for the high surface area. Fig. 2b shows that the HIO sample also consists of spheroidal structures with a similar wide diameter range to the HIOC composite. The higher magnification SEM image (inset of Fig. 2b) shows that the sphere-like structures of the HIO sample are made of small connected nanoparticles. Fig. 2c shows the sphere-like structures of HIOC composite with different morphologies and different diameters, including ball-in-ball structures composed of thin nanosheets. The selected area electron diffraction (SAED) pattern of HIOC composite (inset of Fig. 2c) displays the typical diffuse rings of amorphous carbon and diffraction spots which could be assigned to the polycrystalline α-Fe_2O_3. The high resolution TEM (HRTEM) image (Fig. 2e) was taken from the edge of a piece of broken wall of a hollow structure. The lattice fringes are visible and have different spacings, indicating the polycrystalline nature. The areas marked with red arrows are considered to be amorphous carbon, based on the results from both the Raman spectrum and

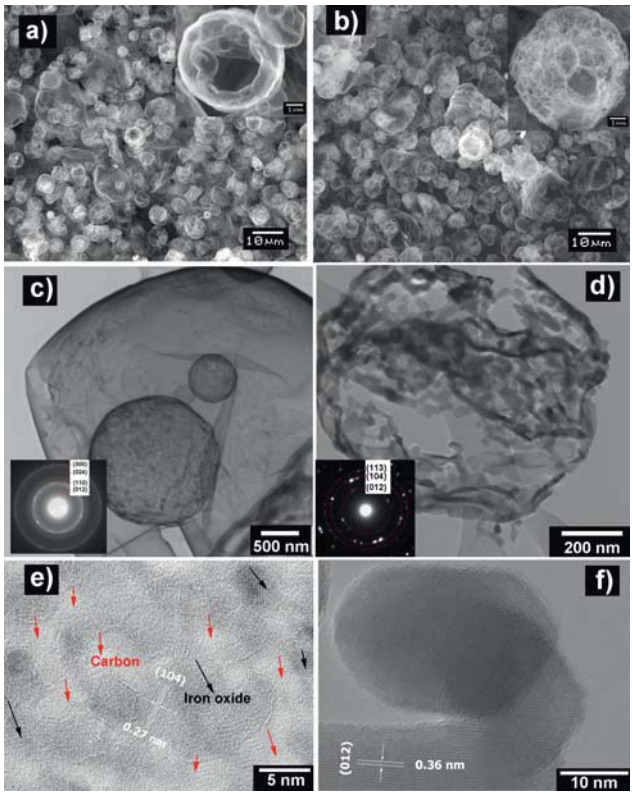

Fig. 2 Typical SEM (a, b), TEM (c, d) and HRTEM (e, f) images of HIOC composite (a, c and e) and HIO (b, d and f). Inset of (c) and (d) are the SAED patterns.

the SAED pattern. It can be seen that the nanocrystals of α-Fe_2O_3 are surrounded by amorphous carbon, indicating the good dispersion of the α-Fe_2O_3 nanocrystals in the carbon-based materials. Fig. 2d shows a TEM image of the HIO sample with hollow sphere-like structures, which is composed of connected small α-Fe_2O_3 nanocrystals with diameters around 20–40 nm. The SAED pattern (inset of Fig. 2d) shows only diffraction spots which can be indexed to polycrystalline α-Fe_2O_3 phase, indicating the good purity of the α-Fe_2O_3. The HRTEM image (Fig. 2f) demonstrates that the lattice fringes are visible, with a spacing of 0.36 nm, which is in good agreement with the spacing of the (012) planes of α-Fe_2O_3.

Different carbon ratios of HIOC composites can be prepared *via* controlling experimental parameters including temperature and concentration of the precursor solution (Table 1). The SEM images (ESI, Fig. S4†) make it clear that the different samples all show similar morphologies, with porous, hollow, spheroidal structures. The BET, XRD (ESI, Fig. S5†), and TGA (ESI, Fig. S1†) results are also summarized in Table 2. The surface areas and crystal sizes as functions of the concentration of iron(II) lactate, the carbon percentage, and the pyrolysis temperature are shown in Fig. 3. It can be seen that the trends in the crystal size curves and surface area curves are reversed. The crystal size increases while the surface area decreases. A low concentration of iron(II) lactate, a low pyrolysis temperature, and high carbon loading favor high surface area and small crystal size.

Table 2 Carbon percentage from TGA, surface area from BET, and crystal size from XRD of different HIOC samples

Sample name	Carbon percentage (%)	BET specific surface area/m^2 g^{-1}	Crystal size/nm
Sample A	—	—	—
Sample B	5.3	265	32.8
Sample C	—	271	31.6
Sample D	—	244	41.0
Sample E	14.7	260	28.8
Sample F	31.2	267	15.8
Sample G	0.6	217	46.9
Sample H	—	191	63.1
Sample I	0	183	149.2

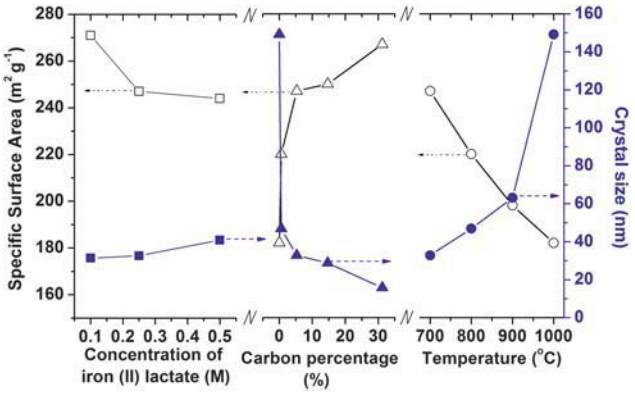

Fig. 3 The surface areas and crystal sizes as functions of the concentration of iron(II) lactate, the carbon percentage, and the pyrolysis temperature.

Electrochemical characterization

Fig. 4 shows the charge-discharge curves for the first 50 cycles of HIOC and HIO electrodes in coin test cells using lithium as the counter and reference electrode between 0.01 and 3.0 V (*vs.* Li^+/Li). All the charge-discharge curves in Fig. 4a and 4b show similar features to those of nanosized α-Fe_2O_3 reported previously in the literature.[8,24] The first discharge curves can be divided into four regions, marked as I, II, III, and IV. From regions I to III, the theoretical capacity of Fe_2O_3 from the reduction reaction of Fe(III) to Fe (0) is 1007 mAh g^{-1}, corresponding to a maximum lithium uptake of 6 Li per Fe_2O_3. The equation is as follows:

$$Fe_2O_3 + 6Li \leftrightarrow 2Fe + 3Li_2O$$

However, both of the electrodes in the initial discharge show specific capacities of more than 1300 mAh g^{-1}, and they still show a high specific capacity of around 1200 mAh g^{-1} for the following several cycles. The extra capacity (region IV) has been explained as the decomposition of electrolyte to form the SEI layer[8] or further lithium storage *via* interfacial reaction due to the charge separation at the metal/Li_2O phase boundary.[25] The high surface area will enhance either/both of the reactions. As a result, the high capacity is observed. It is noticed that the HIOC composite electrode can maintain the reversible capacity (the capacity

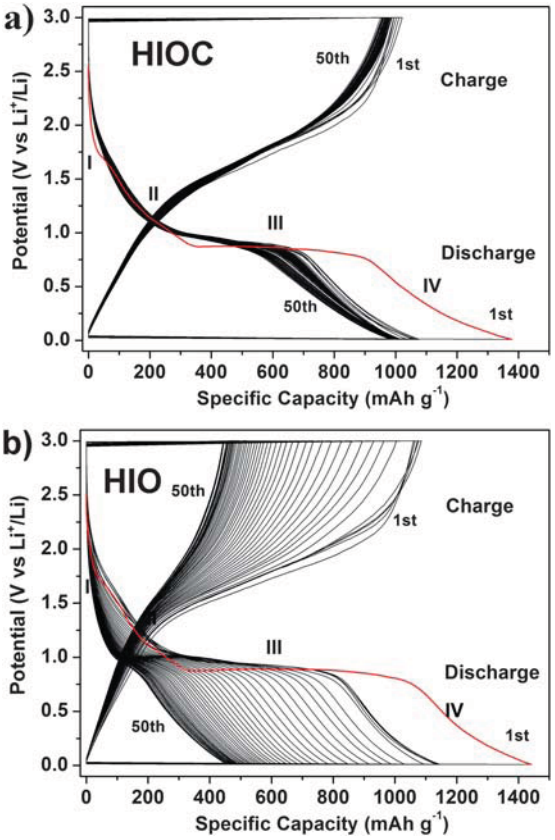

Fig. 4 Typical charge-discharge curves of HIOC nanocomposite electrode (a) and HIO electrode (b). The current densities were 50 mA g^{-1} (0.05 C) for the first five cycles and 100 mA g^{-1} (0.1 C) for the following cycles.

delivered at the 2nd cycle) of around 1000 mAh g^{-1} for 50 cycles, while the HIO gradually loses its reversible capacity to approximately 450 mAh g^{-1} after 50 cycles.

The electrochemical behaviors were further characterized by cyclic voltammograms (CV), as shown in Fig. 5. The initial negative scan results in mainly three peaks (R_1, R_2, and R_3) corresponding to regions I, II, and III. After the first negative scan, the reduction peak only takes the form of one broad peak (R_2'), indicating an irreversible phase transformation during the processes of lithium ion insertion and extraction in the initial cycle. The positive scan shows two peaks (O_1 at 1.6 V and O_2 at 1.9 V). The O_1 and O_2 peaks correspond to the oxidation reactions of Fe(0) → Fe(II) and Fe(II) → Fe(III), respectively.[26] From the 1st cycle to the 5th cycle, the current densities and the positions of peaks O_1 and O_2 in the HIOC composite electrode shown in Fig. 5a are almost the same, indicating the good reversibility of the reaction from Fe(0) to Fe(III), while for the pure hollow α-Fe_2O_3 structures (HIO) (Fig. 5b), the current densities of the O_1 and O_2 peaks decrease gradually, indicating the poorly reversible reaction from Fe(0) to Fe(III). The O_2 peak of HIO electrode is barely seen in the 5th cycle, even in the enlargement of the potential range from 1.25 to 2.25 V *vs.* Li^+/Li shown in the insets of Fig. 5b, indicating that there is no transformation from Fe(II) to Fe(III). The irreversible reaction is likely to be the cause of the capacity loss during the cycling.

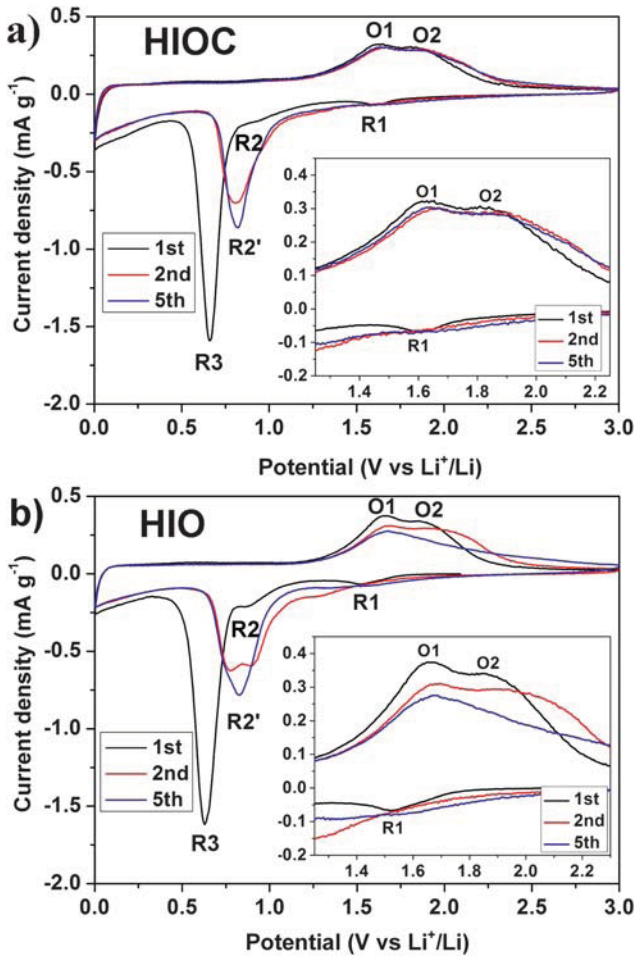

Fig. 5 Typical cyclic voltammograms of HIOC nanocomposite electrode (a) and HIO electrode (b). The insets in the voltammograms show enlargements of particular potential regions. The scan rate of the CV tests was 0.1 mV s^{-1}.

The cycle stabilities of the HIOC nanocomposite and HIO electrodes are shown in Fig. 6. It can be found in Fig. 6a that the specific capacities of HIOC nanocomposites are in the reverse order of the carbon contents in the nanocomposites. The HIOC electrode with 5.3% carbon demonstrates a stable capacity as high as 1210 mAh g^{-1} after 50 cycles which is much better than the other α-Fe_2O_3 materials reported previously,[7–15] such as α-Fe_2O_3 nanospheres (414 mAh g^{-1} for 60 cycles),[12] α-Fe_2O_3 nanotubes (800 mAh g^{-1} for 20 cycles)[9] and microsize α-Fe_2O_3 using CMC as binder (800 mAh g^{-1} for 100 cycles).[10] The performance is even comparable to the silicon-based composite materials,[27,28] which makes the materials more promising for further lithium battery applications. The HIO sample with 0% carbon shows the high capacity of around 1200 mAh g^{-1} for the first 5 cycles, but the capacity starts to drop from the 6th cycle. It only shows a capacity of around 450 mAh g^{-1} at the 50th cycle. Therefore, carbon is an important aspect affecting the cycle life of α-Fe_2O_3.

It is noticed that almost all the previous reports focus on very low rate (about 0.1 C = 100 mA g^{-1}) charge/discharge current densities. It is still a challenge to improve the rate capability of α-Fe_2O_3. Here, changing rates of charge-discharge current densities were also used to investigate the electrochemical performance of different carbon ratios of HIOC, as shown in Fig. 7. It can be seen from Fig. 7a that the capacity of the 0% carbon sample (HIO) dropped rapidly after 5 cycles, even at a relatively low rate of 0.1 C, and reached only around 100 mAh g^{-1} at a current density of 2000 mA g^{-1} (2 C). The HIOC composite with 14.7% carbon shows the highest capacity of around 630 mAh g^{-1} at 2 C. Fig. 7b shows the variation in the cell capacity as a function of the applied rate, expressed in terms of C. The lowest slope indicates the best rate capability. The rate capabilities are in the

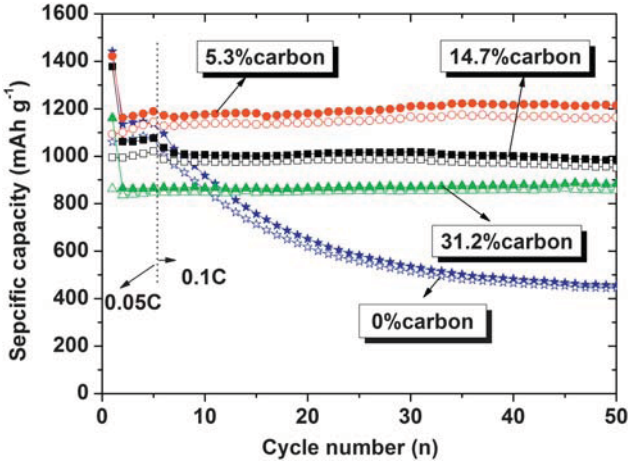

Fig. 6 Cycle life of HIO electrode with carbon percentage of 0% (stars), and HIOC nanocomposites with carbon percentages of 5.3% (circles), 14.7% (squares), and 31.2% (triangles) at a current density of 0.05 C (50 mA g^{-1}) for the first 5 cycles and 0.1 C (100 mA g^{-1}) for the rest of the cycles. The solid and hollow symbols represent discharge and charge capacities, respectively.

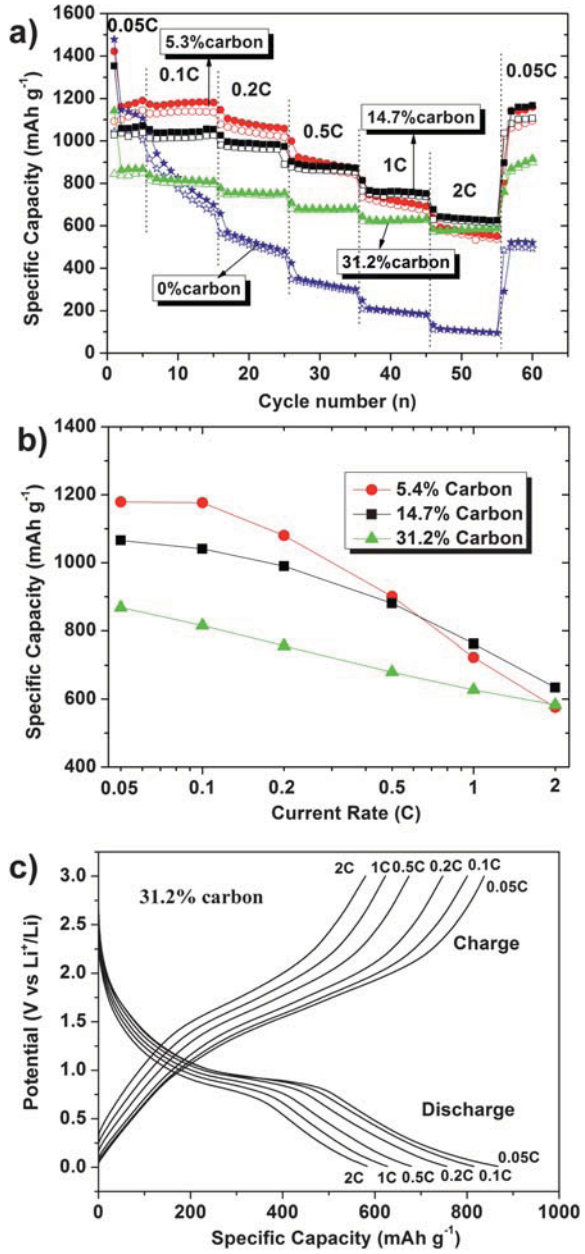

Fig. 7 (a) Rate capabilities of HIO with carbon percentage of 0% (stars), and HIOC composites with carbon percentages of 5.3% (circles), 14.7% (squares), and 31.2% (triangles). The solid and hollow symbols indicate the discharge and charge capacity, respectively. (b) Rate capability plots for HIOC composite electrodes with 5.4% (circles), 14.7% (squares) and 31.2% (triangles) carbon contents. (c) Charge and discharge curves of HIOC with carbon percentage of 31.2% at different current density.

order of HIO with 0% carbon < HIOC with 5.3% carbon < with 14.7% carbon < with 31.2% carbon, which is in the same order as the carbon contents. That is to say the highest carbon content sample (31.2% carbon) shows the best rate capability. Previous reports[15,16] showed that the electron transport to and within the particles is the main factor limiting the rate of iron oxide electrode. Here, the highest carbon content could increase the electron transfer and reduce the resistance within the particles, and such a sample then shows the best rate capability. The charge and discharge curves (Fig. 7c) of HIOC with a carbon percentage of 31.2% from high rate (2C) to low rate (0.05 C) display a similar shape confirming the good high rate capability. After changing the current density back to 0.05 C from 2 C, the capacities of all the HIO and HIOC nanocomposite electrodes increased, instead of dropping, compared with the 5th cycle, showing the good capacity retention of the HIOC electrodes.

The long cycle life of HIOC with 14.7% carbon at 2 C is shown in Fig. 8a. The first 5 cycles were at 0.05 C, and the following cycles were at 2 C. The capacity dropped from the 5th cycle to the 6th cycle due to the change in the rate from 0.05 C to 2 C. From the 10th cycle to the 80th cycle, the capacity dropped from 685 to 560 mAh g^{-1}, then the capacity increased to 730 mAh g^{-1} until the 190th cycle, and the final capacity remained almost the same from the 190th to the 220th cycle. The capacity increase during cycling has also been reported in a previous study.[10] The possible reason would be the processes of activation and stabilization of electrode materials. The HIOC composite electrode shows a capacity of 722 mAh g^{-1} up to 220 cycles, which is much better than in the previous report.[15] The reason is that the high-surface-area hollow structure composed of thin nanosheets can facilitate the contact between active materials and the electrolyte and shorten the lithium diffusion length. Furthermore, the well dispersed small α-Fe_2O_3 nanocrystals in the amorphous carbon can accommodate the volume change caused by lithium insertion and desertion, and could also enhance the electron transport to/within the α-Fe_2O_3 particles or crystals. After cycling, the HIOC nanocomposite electrode can still maintain the sphere-like porous structures (Fig. 8a and 8b), indicating that the hollow-structured α-Fe_2O_3/carbon composite could accommodate the big volume change. Therefore, the high-surface-area carbon

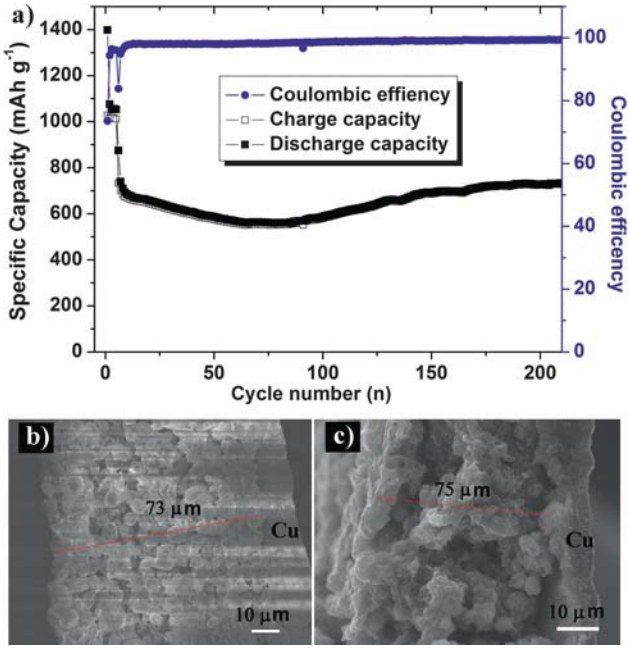

Fig. 8 (a) Cycle stability of HIOC composite (14.7% carbon) electrode at a current density of 0.05 C for the first 5 cycles and 2 C for the rest of the cycles. (b) and (c) SEM images of HIOC nanocomposite electrode before (b) and after (c) cycling taken from the cross-section of the electrode.

composite hollow structure Fe_2O_3 shows enhanced capacity, cycleability, and rate capability. The results are very promising for lithium battery. However, we still need to point out that the initial coulombic efficiency which is 73.5% is relatively low for the lithium-ion cells. The coulombic efficiency of the following cycles is on average around 98.5%. The high coulombic efficiency indicates the potential for industrial applications of HIOC nanocomposite materials. In order to use the as-prepared Fe_2O_3/carbon in total lithium-ion battery, we probably need to lower the surface area to improve the reversible capacity and to reduce the SEI formation and the consummation of electrolyte. The total lithium-ion batteries are going to be assembled using $LiMn_2O_4$ spinel as the cathode and as-prepared Fe_2O_3/carbon as the anode to have a potential of around 3 V.

Conclusions

Hollow-structured α-Fe_2O_3/carbon (HIOC) nanocomposite with a high surface area of around 260 m^2 g^{-1} was synthesized by a one-step, *in situ*, and industrially-oriented spray pyrolysis method using iron lactate and sucrose solution as the precursors. Electrochemical measurements showed that the carbon played an important role in affecting both the cycle life and the rate capability of the electrode. The rate capability becomes better when the carbon content in the composite increases. The HIOC composites showed the best electrochemical performance in terms of high capacity (1210 mAh g^{-1} at 0.1 C), enhanced rate capability and excellent cycle stability with 720 mAh g^{-1} at 2 C up to 220 cycles. The high performance can be ascribed to the novel high-surface-area carbon composite structure which can facilitate the contact between active materials and the electrolyte, enhance lithium and electron transport, and accommodate the volume change. In addition, the HIOC can also be used in other potential applications, such as gas sensors, catalysts, and biomedical applications because it is easily dispersed in water and has a high surface area. The method presented here could also be adopted to synthesize other high-surface-area metal oxide.

Acknowledgements

Financial support provided by the Australian Research Council (ARC) through DP0987805 and ARC Centre of Excellence funding (CE0561616) is gratefully acknowledged. The authors also want to thank Mr R. Davoine and Dr T. Silver for assisting with the BET testing and critical reading of the manuscript, respectively.

References

1 T. B. Reddy and S. Hossain, in *Handbook of batteries*, ed. D. Linden and T. B. Reddy, McGraw-Hill, New York, 3rd edn, 2002, (ch. 35).
2 J. M. Tarascon and M. Armand, *Nature*, 2001, **414**, 359.
3 A. S. Arico, P. Bruce, B. Scrosati, J. M. Tarascon and W. Van Schalkwijk, *Nat. Mater.*, 2005, **4**, 366.
4 P. G. Bruce, B. Scrosati and J. M. Tarascon, *Angew. Chem., Int. Ed.*, 2008, **47**, 2930.
5 J. Chen and F. Cheng, *Acc. Chem. Res.*, 2009, **42**, 713.
6 D. Larcher, S. Beattie, M. Morcrette, K. Edstroem, J. C. Jumas and J. M. Tarascon, *J. Mater. Chem.*, 2007, **17**, 3759.
7 J. Sarradin, M. Ribes, A. Guessous and K. Elkacemi, *Solid State Ionics*, 1998, **112**, 35.
8 D. Larcher, C. Masquelier, D. Bonnin, Y. Chabre, V. Masson, J. B. Leriche and J. M. Tarascon, *J. Electrochem. Soc.*, 2003, **150**, A133.
9 J. Chen, L. Xu, W. Li and X. Gou, *Adv. Mater.*, 2005, **17**, 582.
10 J. Li, H. M. Dahn, L. J. Krause, D. B. Le and J. R. Dahn, *J. Electrochem. Soc.*, 2008, **155**, A812.
11 C. Z. Wu, P. Yin, X. Zhu, C. OuYang and Y. Xie, *J. Phys. Chem. B*, 2006, **110**, 17806.
12 C. Z. Wu, K. Yu, S. Zhang and Y. Xie, *J. Phys. Chem. C*, 2008, **112**, 11307.
13 S. Y. Zeng, K. B. Tang, T. W. Li, Z. H. Liang, D. Wang, Y. K. Wang and W. W. Zhou, *J. Phys. Chem. C*, 2007, **111**, 10217.
14 S. Y. Zeng, K. B. Tang, T. W. Li, Z. H. Liang, D. Wang, Y. X. Qi and W. W. Zhou, *J. Phys. Chem. C*, 2008, **112**, 4836.
15 F. Jiao, J. Bao and P. G. Bruce, *Electrochem. Solid-State Lett.*, 2007, **10**, A264.
16 P. L. Taberna, S. Mitra, P. Poizot, P. Simon and J. M. Tarascon, *Nat. Mater.*, 2006, **5**, 567.
17 Y. G. Guo, J. S. Hu and L. J. Wan, *Adv. Mater.*, 2008, **20**, 2878.
18 Y. G. Guo, Y. S. Hu, W. Sigle and J. Maier, *Adv. Mater.*, 2007, **19**, 2087.
19 S. Basak, D. R. Chen and P. Biswas, *Chem. Eng. Sci.*, 2007, **62**, 1263.
20 J. D. Desai, H. M. Pathan, S. K. Min, K. D. Jung and O. S. Joo, *Appl. Surf. Sci.*, 2006, **252**, 8039.
21 B. K. McMillin, P. Biswas and M. R. Zachariah, *J. Mater. Res.*, 1996, **11**, 1552.
22 D. L. A. De Faria, S. V. Silva and M. T. De Oliveira, *J. Raman Spectrosc.*, 1997, **28**, 873.
23 F. Jiao, A. Harrison, J. Jumas, A. V. Chadwick, W. Kockelmann and P. G. Bruce, *J. Am. Chem. Soc.*, 2006, **128**, 5468.
24 X. L. Wu, Y. G. Guo, L. J. Wan and C. W. Hu, *J. Phys. Chem. C*, 2008, **112**, 16824.
25 J. Jamnik and J. Maier, *Phys. Chem. Chem. Phys.*, 2003, **5**, 5215.
26 J. Morales, L. Sanchez, F. Martin, F. Berry and X. L. Ren, *J. Electrochem. Soc.*, 2005, **152**, A1748.
27 S. H. Ng, J. Z. Wang, D. Wexler, K. Konstantinov, Z. P. Guo and H. K. Liu, *Angew. Chem., Int. Ed.*, 2006, **45**, 6896.
28 Y. S. Hu, R. Demir-Cakan, M. M. Titirici, J. O. Muller, R. Schlogl, M. Antonietti and J. Maier, *Angew. Chem., Int. Ed.*, 2008, **47**, 1645.

